JOURNAL OF AIRCRAFT
Vol. 39, No. 5, September–October 2002

Axial Detection of Aircraft Wake Vortices Using Doppler Lidar

Michael Keane,* Daniel Buckton,* and Michael Redfern*
National University of Ireland, Galway, Ireland
Christoph Bollig,† Carsten Wedekind,† and Friedrich Köpp†
Deutsches Zentrum für Luft- und Raumfahrt,
DLR, German Aerospace Research Center, 82230 Wessling, Germany
and
Francois Berni‡
SEXTANT, 26027 Valence Cedex, France

The real-time detection of aircraft wake vortices has become an important part of studies aimed at increased runway productivity. A processing approach is presented, which has been used to detect wake vortices from an axial point of view with a Doppler lidar system. The performance of the processing approach is investigated using simulation techniques. In addition, the effectiveness of the approach is demonstrated using data from a series of wake vortex measurement experiments carried out at Toulouse airport in March 2000. Robust axial detection of wake vortices with a Doppler lidar system has been achieved at ranges between 400 m and 2 km. Sample results for Airbus A340- and Airbus A320-generated wake vortices are presented.

Nomenclature

$\hat{c}_k$	=	confidence level of mean radial velocity estimate
$\hat{e}_{i,j}$	=	rectilinearly distributed estimate
$\hat{e}_k$	=	sinusoidaly distributed estimate
f_0	=	lidar output frequency corresponding to 0-m/s Doppler shift
$\hat{f}$	=	mean frequency estimate
$k_{\max}$	=	index of peak component of periodogram
$P(n)$	=	periodogram coefficient
$P_{\text{sig}}(n)$	=	periodogram coefficient after noise floor removal
SNR_w	=	wideband signal to noise ratio
T_s	=	sampling frequency
$\hat{v}$	=	mean radial velocity estimate
w	=	spectral width due to the temporal profile of the lidar pulse
$\boldsymbol{x}_{i,j}$	=	coordinates of constructed rectilinear grid
$\boldsymbol{x}_k$	=	coordinates of sinusoidaly distributed estimates
y_k	=	range gate samples
Δf	=	frequency resolution of periodogram
λ	=	wavelength of lidar pulse
$\hat{\sigma}$	=	spectral width estimate

I. Introduction

WAKE vortices are rotating columns of turbulent air, shed from the wingtips of all aircraft and left behind in their wake.[1] The wake vortices shed by one aircraft can pose a serious threat to any following aircraft encountering them.[2] The main hazard associated with wake vortex encounter occurs if the following aircraft flies along the axis of rotation of a wake vortex from a leading aircraft. If this occurs, the vortex can effect a potentially hazardous rolling moment on the following aircraft.[3] During takeoff and touchdown, an aircraft is in a low-airspeed, low-altitude state and may be unable to recover from such an encounter.

Currently, encounters with hazardous wake vortices are avoided by imposing a longitudinal separation of aircraft during the landing and takeoff phases of flight. Aircraft are categorized according to their rated maximum takeoff weights, and the minimum longitudinal separation distances are prescribed according to the weight classification of the leading and following aircraft in the pair. With air traffic growth far exceeding the growth of new facilities, an increasing number of airports are becoming capacity saturated.[4] In response, researchers have been encouraged to develop technology that will allow existing airports to increase capacity without compromising passenger safety.

The real-time detection of aircraft wake vortices has become an important part of studies aimed at increased runway productivity.[5] A number of ground-based lidar systems have demonstrated remote lateral detection of aircraft wake vortices.[6,7] All of these systems have consisted of lidar measurements in a vertical scan plane, oriented perpendicular to the flight path. This lateral configuration allows wake vortices to be detected via the Doppler shifts caused by their characteristic rotational components.

Whereas ground-based detection of wake vortices is best achieved from a lateral point of view, an airborne wake vortex detection system must be capable of detecting wake vortices from an axial point of view because the main hazard is associated with axial encounter. An airborne wake vortex detection system must be forward looking to provide the pilot with some advance warning of vortex encounter. If a Doppler lidar were to be used in such a forward looking detection system, the lidar orientation would be closely aligned with the axis of the rotation of the wake vortex, so that the characteristic rotational component would not be directly detectable because it is perpendicular to the propagation of the radiation. Hence, axial detection of wake vortices with a Doppler lidar system requires a different approach to that used in lateral detection systems. Previously published[8] simulation results have indicated that aircraft wake vortices may be detectable from a close to axial point of view. Those early results prompted further research by a European consortium,[9] which culminated in a series of wake vortex measurement from a close to axial point of view with a ground-based Doppler lidar.

During February and March of 2000, a Doppler lidar system with a two-dimensional scanner was situated under the glide slope of landing aircraft. The scanner was oriented back along the glide slope to capture mainly the axial components of the wake vortices. Robust detection of vortices from many types of commercial aircraft was achieved. To the knowledge of the authors, this paper is the first

Received 18 August 2000; revision received 9 September 2001; accepted for publication 8 May 2002.

*Senior Researcher, Department of Experimental Physics.
†Senior Researcher, Institute of Optoelectronics, Oberpfaffenhofen.
‡Senior Engineer, 25, rue Jules Védrines.

in which remote detection of aircraft wake vortices from a close to axial point of view has been demonstrated.

In Sec. II, we present an introduction to coherent Doppler lidar and in Sec. III describe the approach that was used to develop the processing algorithms used in the detection experiments. Sections IV and V present the processing algorithms used and the algorithm performance in simulation experiments. In Sec. VI, the ground-based lidar measurement experiments are described and samples results are presented for number of cases. Conclusions are drawn in Sec. VII.

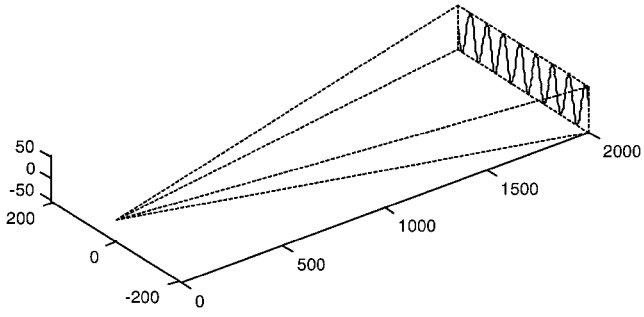

Fig. 1 Schematic of the sinusoidal scanning pattern at 2000-m range, where axes are in meters. For clarity, the number of sinusoidal cycles per scan as been reduced (Table 1).

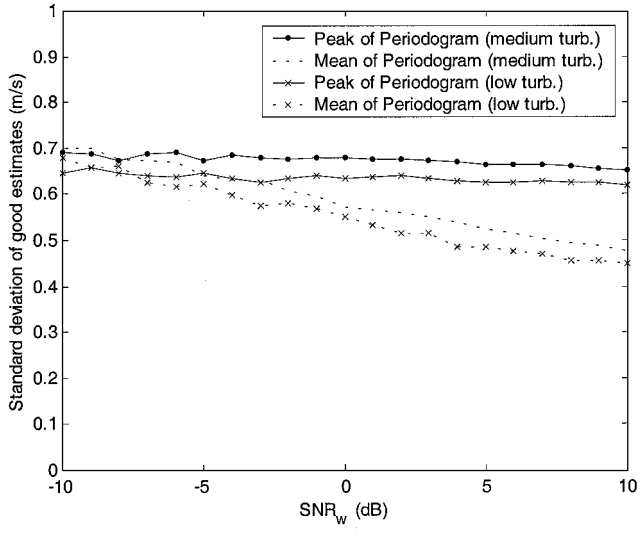

a) Standard deviation of the good estimates

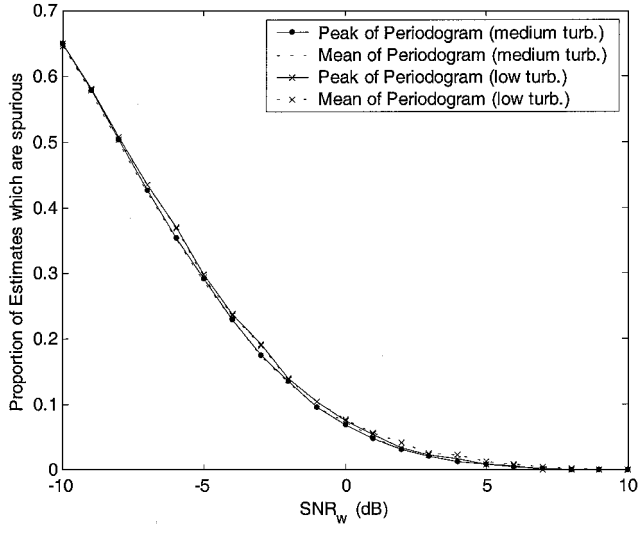

b) Proportion of spurious estimates vs wideband SNR

Fig. 2 Performance of mean velocity estimators vs wideband SNR.

II. Atmospheric Measurement with Coherent Doppler Lidar

Lidar is an acronym derived from light detection and ranging and is a concept similar to radar. Atmospheric Doppler lidar systems use optical instrumentation to transmit coherent, narrowband, laser pulses into the atmosphere along a narrow path known as a line of sight (LOS). As each optical pulse travels out along the LOS, it encounters a distributed ensemble of aerosol particles. These particles reflect a portion of the incident light back along the LOS. At optical wavelengths, the bulk of the backscattered light is contributed by particles with diameters less than 3 μm; these particles are small enough to be advected by the wind and thus serve as effective wind tracers.[10] The light backscattered by an aerosol is Doppler shifted by a frequency $f = -2v/\lambda$, where v is the radial component of wind velocity, that is, the velocity component parallel to the direction of propagation of the pulse, and λ is the wavelength of the transmitted pulse.

Because the scatterers form a distributed target, a continuous backscattered signal is present at the system receiver as the pulse propagates away from the lidar. This backscattered signal is optically mixed with light from a reference laser at the surface of a photodetector. This optical mixing, known as heterodyning, translates the Doppler shift down into the radio frequency range, allowing conversion to an electrical signal by the photodetector. Sampling and range-gating of the photodetector signal allow for range-resolved analysis of the backscattered signal.

The use of a two-dimensional scanner, to move the LOS between pulses, facilitates three-dimensional atmospheric measurement. With such an approach, it is desirable to scan the entire field of view (FOV) in less than a few seconds; otherwise the atmosphere will have changed significantly during the scan time. This necessitates the use of a Doppler lidar with a high-pulse-repetition frequency coupled to a high-speed scanner.

III. Algorithm Development Approach

In a Doppler lidar, only the component of the air velocity in the direction of propagation of the lidar beam causes a Doppler shift in the returned signal. Hence, it is not possible to directly detect the rotational velocity component of a wake vortex while viewing it axially. Consequently, axial detection of wake vortices with a

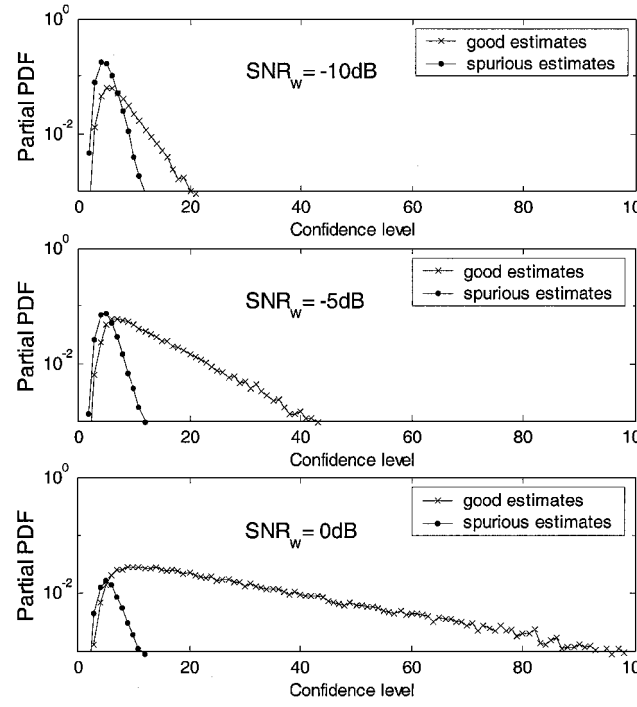

Fig. 3 Partial PDFs of the confidence level at SNR$_w$ of − 10, − 5 and 0 dB; partial PDFs are generated by separately plotting the density of confidence levels for good and spurious estimates.

Doppler system relies on the presence of identifiable axial Doppler signatures. Such signatures may be axial velocity components or axial turbulence within or near to the vortex core.

The generation of an axial velocity in the core as part of wake vortex rollup has been explained theoretically by Brown.[11] However, this initial axial velocity holds only at relatively short distances behind the wing, where the spiral system is well rolled up, but before the vortex has spread and been reduced in intensity by turbulent diffusion. Much farther back from the wing, the development of axial velocity characteristics in the vortex core, as a result of axial pressure gradients, has been predicted theoretically by Batchelor.[12]

To investigate the feasibility of axial detection, large-eddy simulations (LES) techniques were used to simulate the evolution of wake vortices in different turbulence conditions. The three-dimensional flowfields from the LES were applied to a time-domain simulation of a Doppler lidar system.[8] Other inputs to the Doppler lidar simulation system are the lidar performance parameters, the atmospheric

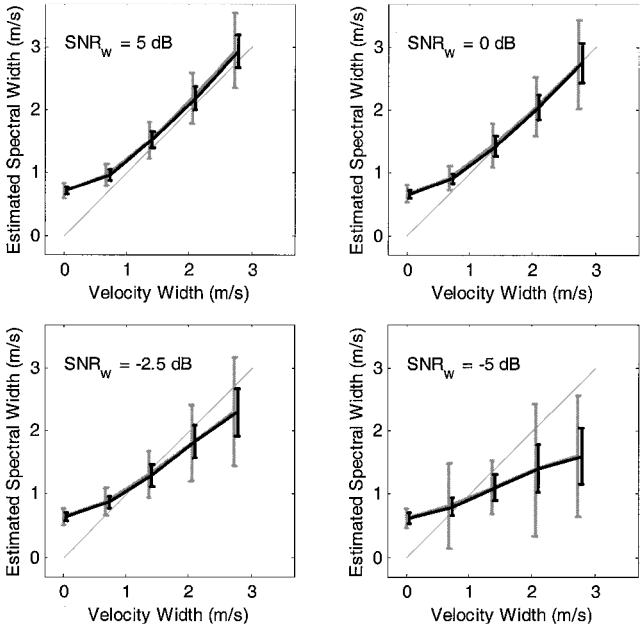

Fig. 4 Gray error bars indicate the mean and standard deviation of the velocity spectral width estimator vs true velocity width in a 225-m range gate, black error bars summarize the spectral width estimate accuracy after applying the spectral width image processing algorithm. Note that for clarity, the image processing results have been shifted by 0.05 m/s along *x* axis.

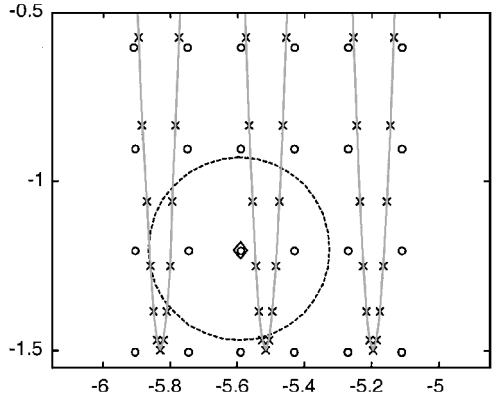

Fig. 5 Angular distribution of LOS from a sinusoidal scanner × and the rectilinear positions used in the image processing ○. Sinusoidally distributed estimates within the indicated region are inputted to the operation *F*, to generate the estimate at the position marked by ◇. For clarity, the shot density is half of the actual shot density. Axes are in degrees.

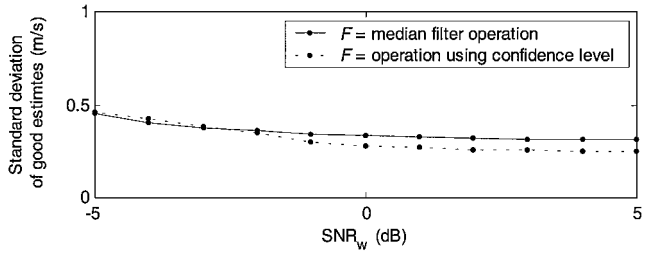

a)

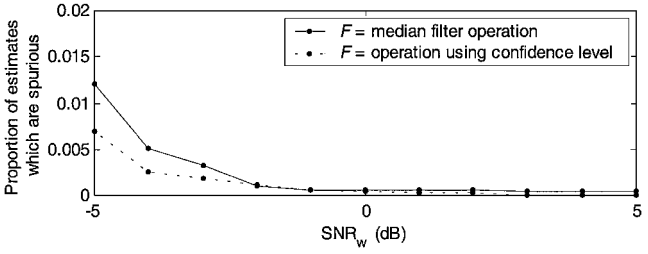

b)

Fig. 6 Performance of the mean velocity image processing algorithm: a) standard deviation of the good estimates after image processing and b) proportion of spurious estimates after image processing.

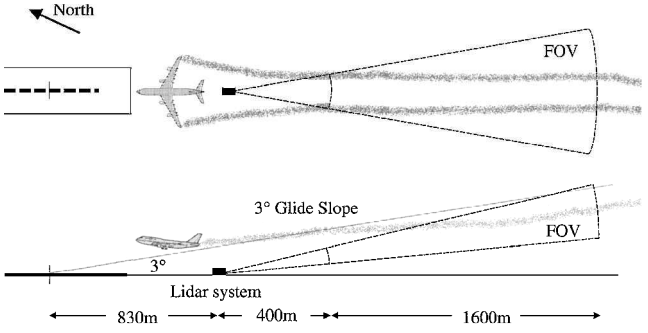

Fig. 7 Plan view and elevation of the ground-based wake vortex measurements showing the instrument landing system glide slope and of the lidar system's FOV.

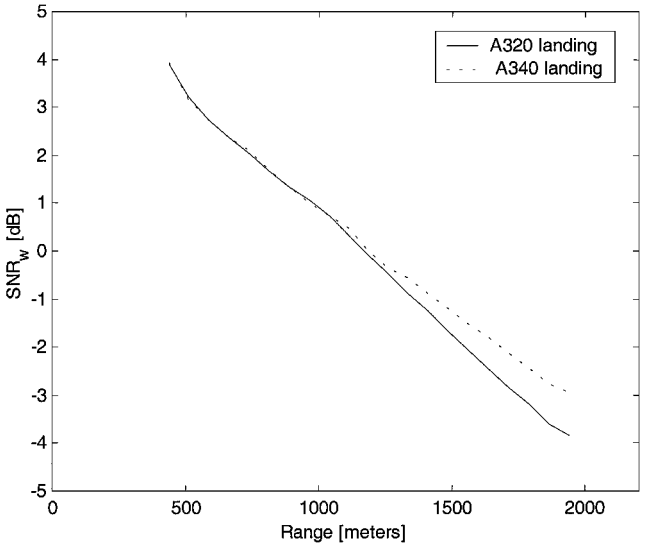

Fig. 8 Estimated wideband SNR vs range for the A320 and A340 cases.

parameters, the scanning pattern and the measurement geometry. Darracq et al.[8] gives a full description of the simulation process.

The simulation experiments were used to define the parameters of a Doppler lidar system capable of detecting wake vortices from an axial point of view. Early results indicated that a lidar pulse length of about 400 ns and a transverse spatial resolution of 6 m or better would be required to achieve axial detection. Ideally, the two-dimensional scanner would generate a rectilinear scanning pattern with an equal angular density of lidar shots throughout the field of view. However, such a scan pattern is difficult to realize mechanically. Further simulation experiments indicated that the mechanically feasible sinusoidal scan pattern shown in Fig. 1, is capable of providing the required scanning density.

Simulation experiments were also used to develop candidate processing algorithms. A two-stage processing approach was developed. The first stage, the signal-processing stage, involves estimating the mean radial velocity and the spectral width at various ranges along each LOS. The second stage, the image-processing stage, is applied to the results of signal-processing stage and aims to eliminate signal-processing noise while preserving wake vortex Doppler signatures.

IV. Signal Processing

The aim of signal processing is to estimate the mean radial velocity and the spectral width[13] at various ranges along each LOS. For this application, mean radial velocity estimation is carried out over 75-m range gates, while spectral width estimation is carried out over 225-m range gates. This approach is appropriate because accurate range resolution of radial velocity estimates is desired to capture the axial structure of the vortices. For spectral width estimation, however, a longer range gate is used so that larger scale axial turbulence and axial flows associated with the vortices can be captured.

The signal to noise ratio (SNR), defined as the ratio of the average heterodyne signal power to the average noise power, is a parameter that affects signal-processing performance. In this study, real sampling of the photodetector signal at 128 MHz is used in both the simulation experiments and the ground-based measurements. This implies a noise bandwidth of 64 MHz. For clarity, the label SNR_w is used to emphasise that the wideband SNR is being used.

Both mean radial velocity and spectral width estimation are carried out in the spectral domain via the periodogram. The periodogram of the samples from a given range gate is an estimate of the spectrum of the Doppler signal from that range gate plus the noise associated with the heterodyne detection process. This is defined as

$$P(n) = \frac{1}{N}\left|\sum_{k=0}^{N-1} y_k \exp\left(-\frac{2\pi i k n}{N}\right)\right|^2$$

where $P(n)$ is an estimate of the power at frequency given by the product $n\Delta f$ and $\Delta f = 1/NT_s$ is the frequency resolution of the

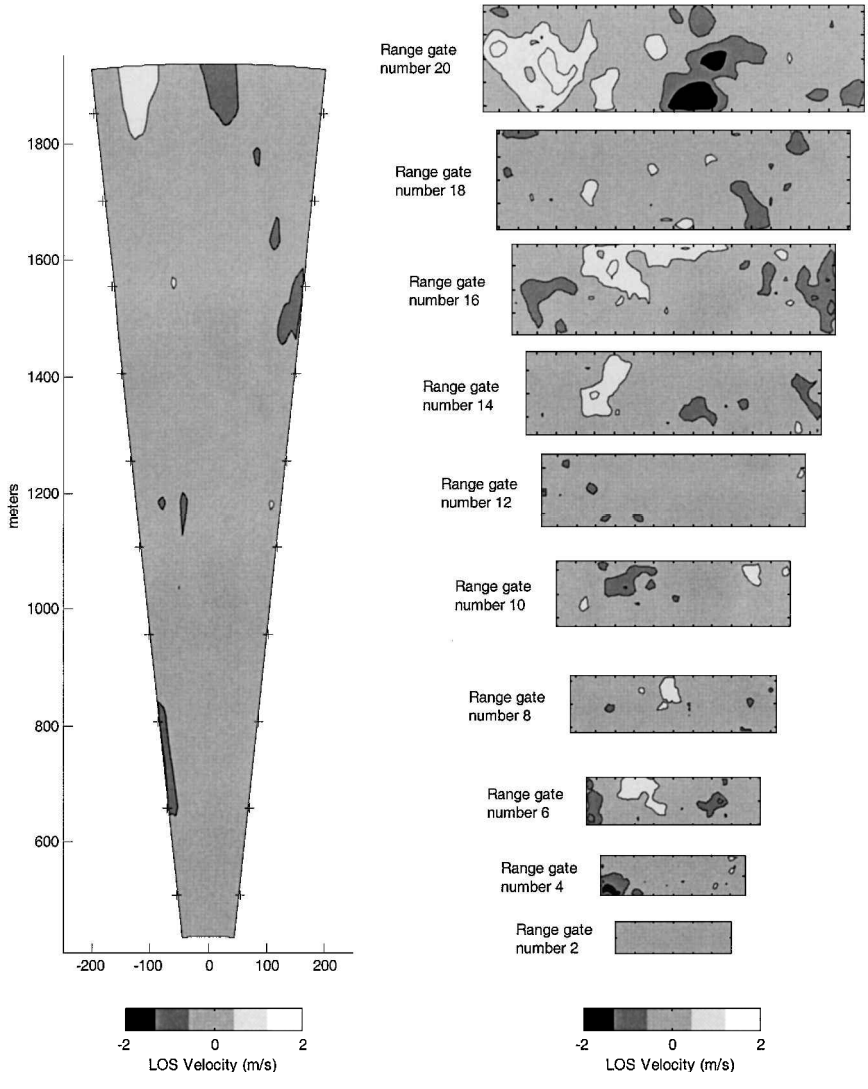

Average top view of the mean radial velocity

Individual range gate images

Fig. 9 Mean radial velocity images for background wind case; + mark centers of range gate images and marks on the axes of the range gate images separated by 20 m.

periodogram. Zero padding of the input sequence may be used to increase N and decrease Δf (Ref. 14).

The average spectral noise floor, due to the heterodyne detection process, is subtracted from the periodogram to generate an estimate of the Doppler signal spectrum. Because real sampling of the photodetector signal is used, only the first half of the spectrum is unique. Therefore, P_{sig} is defined as the first half of the estimated Doppler signal spectrum (noise floor removed). The following sections describe the calculation of the mean Doppler velocity and the Doppler velocity spectrum width from P_{sig}.

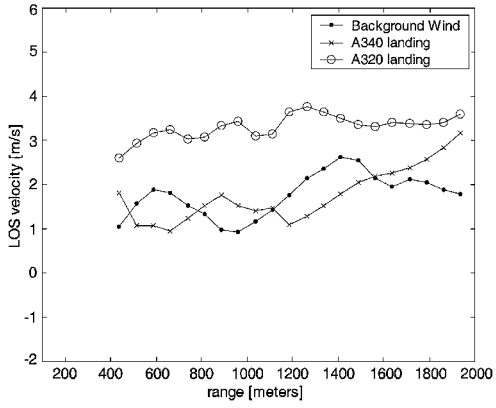

Fig. 10 Radial velocities subtracted from range gate images before display.

A. Mean Radial Velocity Estimators

An estimate of the mean radial velocity $\hat{v}$ is calculated from the mean Doppler frequency estimate $\hat{f}$ using the conversion $\hat{v} = -(\hat{f} - f_0)\lambda/2$, where λ is the wavelength of the Doppler lidar and f_0 is the lidar output frequency corresponding to a 0-m/s Doppler shift.

The estimated mean frequency $\hat{f}$ of the periodogram of a real sampled signal is calculated from P_{sig} as

$$\hat{f} = \frac{1}{NT_s}\left(k_{\max} + \frac{\sum_{k_{\max}-N/4}^{k_{\max}+N/4}(k-k_{\max})\,P_{\text{sig}}[\text{mod}_{N/2}(k)]}{\sum_{k=0}^{N/2}P_{\text{sig}}(k)}\right)$$

where $k_{\max}$ is a first approximation of the mean, generated by taking the index of the peak of the periodogram. Calculating the mean frequency around $k_{\max}$ eliminates bias toward the center of the bandwidth.[13] Simulation results have shown that for narrowband signals the accuracy of this estimator can be significantly improved by confining the summation to the spectral region corresponding to ± 4 m/s from the peak estimate. This reduces the effect of any spurious noise peaks on the estimator accuracy.

If the bandwidth of the signal is small compared to the bandwidth of the system, the peak of the periodogram can give a good estimate

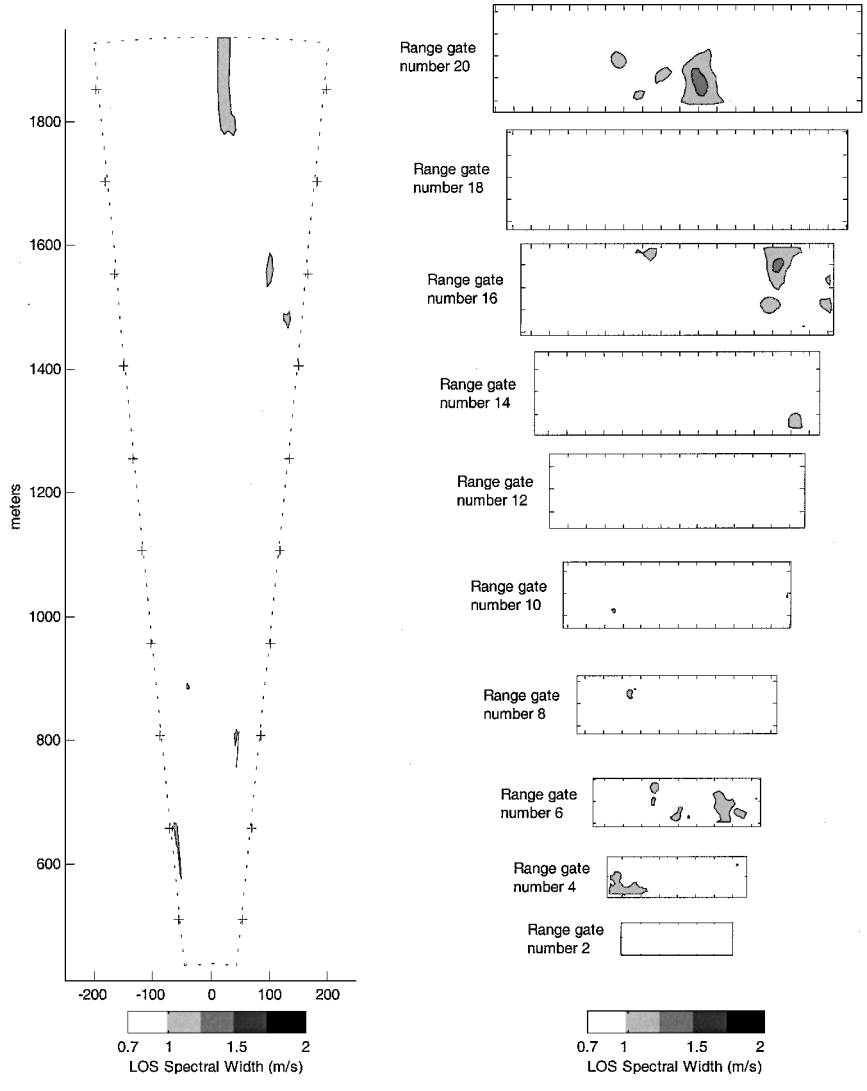

Average top view of spectral width **Individual range gate images**

Fig. 11 Spectral width images for background wind case; average + mark centers of range gate images and marks on axes of range gate images are separated by 20 m.

of the mean frequency. This computationally efficient estimate is given by

$$\hat{f} = k_{\max}/NT_s$$

The accuracy of this method is limited by the frequency resolution of the discrete periodogram. Therefore, zero padding is used to increase N and decrease Δf.

B. Mean Velocity Estimation Accuracy

The performance of an unbiased mean velocity esimator is fully described by the probability density function (PDF) of its estimator error. For unbiased estimators, the PDF is characterized by a uniform distribution of spurious estimates throughout the velocity search space and a local Gaussian distribution of good estimates centered on the true mean velocity.[15]

The performance of a mean velocity estimator depends on the SNR at the photodetector and the turbulence in the range gate scattering volume. Frehlich[15] has identified two regimes that describe Doppler lidar performance: the pulse dominated regime, in which atmospheric turbulence along the range gate is negligible, and the atmospheric regime, in which the atmospheric variation along the range gate affects velocity estimation accuracy. Algorithm performance has been investigated in both regimes.

Wind fields containing negligible turbulence were generated using Kolmogorov scaling (see Ref. 15) with outer scales of 1000 m and an energy dissipation rate of 10^{-5} m^2/s^3, and wind fields containing significant turbulence were generated using with the same outer scale and an energy dissipation rate of 10^{-3} m^2/s^3. A time-domain lidar simulation method[16] was used to generate lidar shots at various wideband SNR levels from the Kolmogorov wind fields.

The two mean radial velocity estimators were applied to independent 75-m range gates for all of the simulated signals. The pulse weighted mean radial velocity[15] averaged over the range gate was subtracted from the estimated mean radial velocity to generate the estimator error. A Gaussian function on a uniform background has been fitted to each estimator error PDF to estimate the standard deviation of the good estimates around the true mean and the proportion of estimates, which are spurious. The results are presented in Fig. 2.

Figure 2b shows that the decrease in the proportion of spurious estimates with increasing SNR_w is similar for the two mean velocity estimators investigated here. At an SNR_w of -10 dB, it can be seen that almost 65% of the velocity estimates are spurious, whereas at an SNR_w of $+10$ dB, less than 1% of the estimate are spurious.

Figure 2a shows that atmospheric turbulence has a weak effect on the accuracy of the estimators, that is, medium level turbulence within the range gate increases the standard deviation of the good estimates. In both turbulence regimes, the periodogram mean

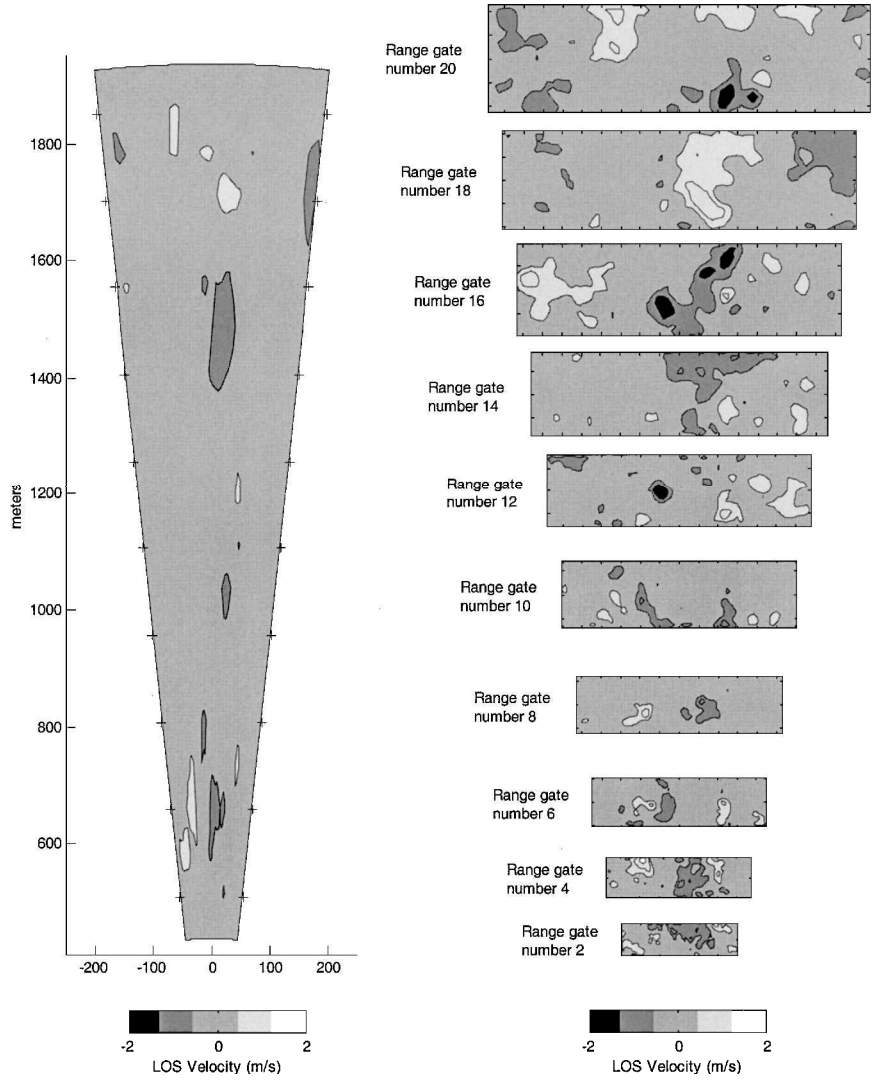

Average top view of the mean radial velocity

Individual range gate images

Fig. 12 Mean radial velocity images from scan 5 during Airbus 340 landing; + mark centers of range gate images and marks on the axes of range gate images are separated by 20 m.

estimator performs slightly better than the computationally efficient periodogram peak estimator, particularly at higher SNR_w.

C. Confidence of the Estimate

Signal statistics dictate that a certain proportion of the velocity estimates will be spurious. Understanding the mechanism that causes spurious estimates offers an approach through which the level of confidence associated with a given estimate can be calculated. For spectral estimators, spurious estimates result when the signal power drops due to "fading," and a noise peak is mistakenly identified as the signal component. Conversely, good estimates are generated when the signal power spectrum is identifiably above the noise spectrum.

The average energy in the spectral region around the estimated mean frequency, given by $\hat{f} \pm w$, can be used to calculate the confidence level associated with a given estimate. The parameter w is the spectral width due to the transmitted pulse shape and is given by $w = 1/\sqrt{8\pi\sigma}$, where σ is the $1/e$ half-width of the transmitted pulse.[15] When a spurious estimate is generated, this confidence level will be low because the region $\hat{f} \pm w$ will contain only noise. However when a good estimate is generated, the region $\hat{f} \pm w$ will contain the signal, so that the confidence level for good estimates would be expected to be higher than that for spurious estimates.

Figure 3 contains partial PDFs of the confidence level of the peak of the periodogram mean estimator at various SNR_w. Note, that the scaling on the x axis is arbitrary. The results indicate that the confidence level is related to the estimation accuracy. Good estimates are classified as those that fall within 2 m/s of the true mean velocity. The sum of the partial PDFs generates the true PDF of the confidence level. The confidence level is below 12 for almost all of the spurious estimates, whereas most good estimates have a confidence level that is above 12 for SNR_w of -5 dB and above. In general, the higher the confidence levels, the more likely it is that the estimate is good. Thus, the confidence level can be used in the image-processing stage to identify estimates that are highly likely to be spurious.

D. Velocity Spectral Width Estimation

The spectral width is a measure of the velocity variation over the range gate volume and is related to the level of turbulence or the shear within the volume.[17] For a real sampled signal, the estimated velocity spectral width estimate $\hat{\sigma}$ of a range gate is calculated from P_{sig} as

$$\hat{\sigma} = \frac{\lambda}{2NT_s}\sqrt{\frac{\sum_{k=k_1}^{k_2}(k/N - \hat{f}T_s)^2 P_{\mathrm{sig}}[\mathrm{mod}_{N/2}(k)]}{\sum_{k=k_1}^{k_2} P_{\mathrm{sig}}(k)}}$$

where $\hat{f}$ is the estimated mean radial frequency of the periodogram used for spectral width estimation, N is the number of discrete frequency points in the periodogram, and mod is the modulus operation. The summation is tightly limited to the signal lobe because inclusion of any noise spikes in this calculation will bias the estimate

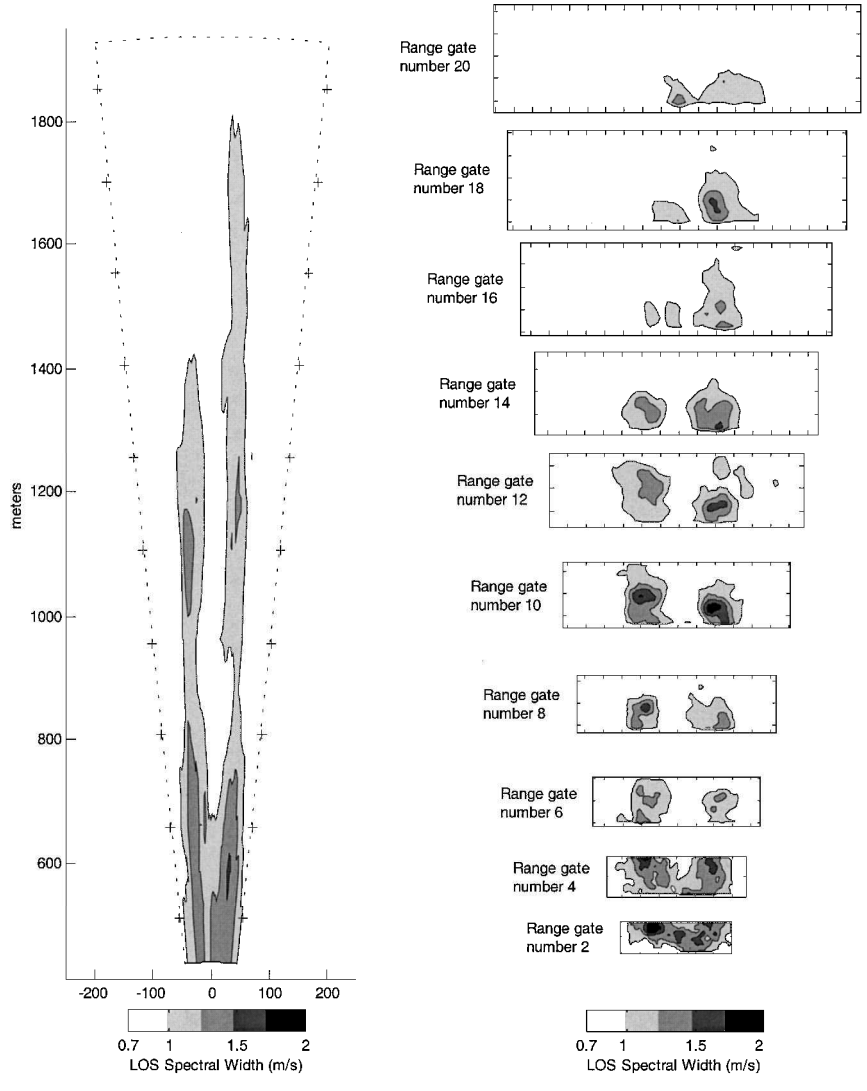

Average top view of the spectral width **Individual range gate images**

Fig. 13 Spectral width images from scan 5 during Airbus 340 landing; + mark centers of range gate images and marks on axes of range gate images are separated by 20 m.

high. Therefore, the extremities of the signal lobe, labeled k_1–k_2, are identified before implementing the preceding equation.

The periodogram coefficients at any frequency are exponentially distributed, regardless of the number of data points in the transform.[17] This randomness contributes to considerable inaccuracy in the spectral width estimates even at high SNR_w. To reduce this effect, spectral averaging is carried out with P_{sig} from the corresponding range gate of the previous and the following shots. The velocity spectral width estimate is then calculated from the three-shot averaged P_{sig} as defined earlier.

E. Velocity Spectral Width Estimator Performance

To investigate the velocity spectral width estimator performance, a large number of lidar signals were simulated from wind fields containing velocity shears using a time-domain simulation method.[16] The spectral width estimator was applied to the three LOS average P_{sig} generated from 225-m range gates. The estimated spectral widths are compared with the velocity width[17] calculated from the point velocities and the results are plotted in Fig. 4. In each case, the mean estimated spectral width has been plotted along with an error bar, which indicates the standard deviation of the estimates. Figure 4 summarizes the spectral width estimator performance over a range of spectral width values and at various SNR_w levels. The spectral width estimator performs well at SNR_w of -2.5 dB and above because it accurately reflects the underlying velocity width, whereas at -5 dB, the spectral width estimator underestimates the underlying velocity width. At all SNR_w levels, the estimator is biased high at widths less than 0.7 m/s. This effect is due to the inherent spectral width of the transmitted pulse broadened by the spectral shape of the rectangular window. This combination effectively sets a minimum value on the estimated spectral width.

V. Image Processing

A. Rectilinearization and Image Construction

Mean radial velocity and spectral width estimates from all range gates that are equidistant from the lidar are used to generate transverse range gate images. If a rectilinear scanning scheme was employed, the construction of these images would be straightforward because each mean velocity and spectral width estimate could be mapped to pixels in a rectilinear mean velocity and spectral width range gate image, respectively. A sinusoidal scanning pattern, however, results in a highly nonlinear spatial distribution of estimates and does not facilitate image processing or image display. Therefore, an approach has been developed that converts the sinusoidally distributed velocity and spectral width estimates into sets of rectilinearly distributed velocity and spectral width estimates, while simultaneously allowing the implementation of noise reduction algorithms.

For each set of range gates equidistant from the lidar, a rectilinear grid spanning the field of view with coordinates $\boldsymbol{x}_{i,j}$ is generated. All estimates within a distance d of $\boldsymbol{x}_{i,j}$ are used to generate an estimate at $\boldsymbol{x}_{i,j}$. That is,

$$\hat{e}_{i,j} = F(\hat{e}_k) \qquad \forall k$$

such that $|\boldsymbol{x}_k - \boldsymbol{x}_{i,j}| < d$, where $\hat{e}_k$ are the sinusoidally distributed estimates (either mean velocity or spectral width), $\hat{e}_{i,j}$ are the resulting rectilinearly distributed estimates, and F is the image-processing operation. The distance d defines the radius of the image-processing operation, as shown in Fig. 5. To adapt the image processing to the decrease in spatial resolution with range from the lidar, the distance d can be adjusted with range.

The operation F can be any operation that chooses the best estimate to represent position $\boldsymbol{x}_{i,j}$ from the set of available estimates $\hat{e}_k$. The simulation results indicate that the error statistics from mean velocity estimation and spectral width estimation result are quite different. Therefore, different image-processing operations are used for each image set.

B. Radial Velocity Image Processing

The confidence level associated with each velocity estimate is incorporated into the mean velocity image processing. For the mean radial velocity estimates the operation F is defined as follows:

$$F(\hat{v}_k, \hat{c}_k) = \mathrm{mean}(\hat{v}_k) \qquad \forall k$$

subject to $\hat{c}_k > c_T$, where c_T is a confidence level threshold which rejects almost all spurious velocity estimates. If no estimates have a confidence level above the chosen threshold, then the algorithm takes the median of all of the available velocity estimates.

The performance of the mean radial velocity image processing is summarized in Fig. 6. Figure 6 shows that the algorithm, which includes the confidence level of the estimate, eliminates all of the spurious estimates at SNR_w levels down to -5 dB. Comparison with Fig. 2 illustrates the improvement in velocity image accuracy due to the image-processing algorithm. For example, at an SNR_w of -5 dB, Fig. 2 shows that the proportion of spurious estimates generated by the signal-processing stage is approximately 30%. After image processing, only 0.7% of the velocity estimates are spurious, and the standard deviation of the good estimates is halved.

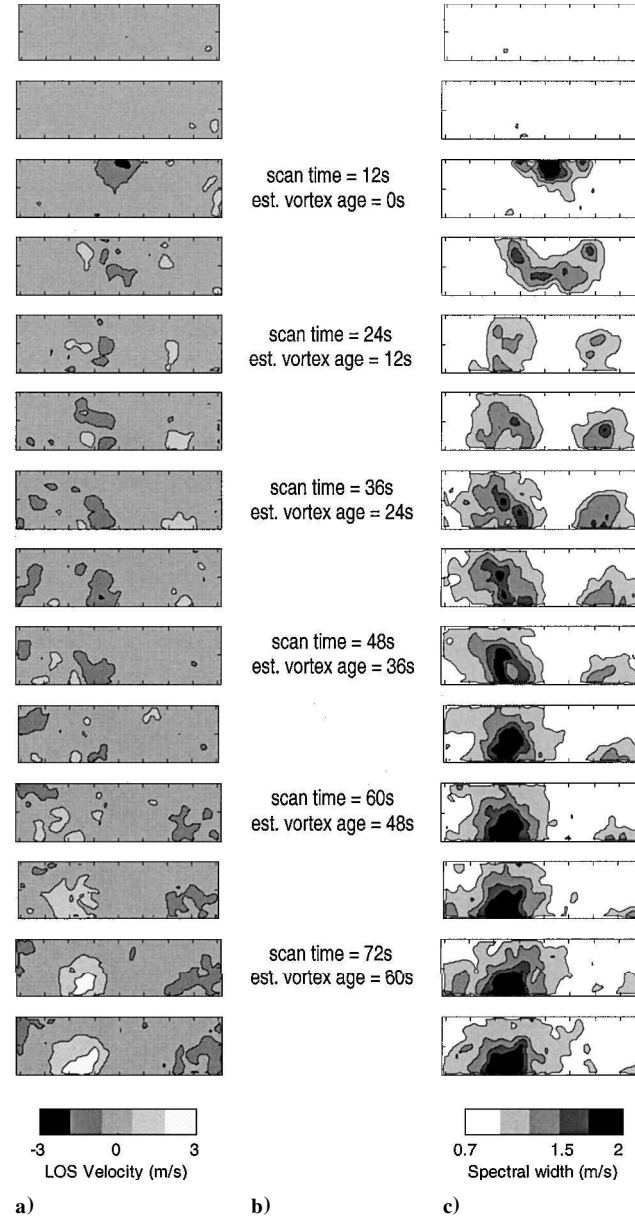

Fig. 14 Time evolution of images from range gate 6, centered 812 m from lidar system, during an Airbus 340 landing; marks are 20 m apart on both axes: a) mean radial velocity variation from average range gate velocity, b) approximate start time of each scan and estimated vortex age (estimated from the flyby time) and c) spectral width.

For comparison, the performance of the operation F defined as $F(\hat{v}_k) = \text{median}\ (\hat{v}_k)$ is included in Fig. 6. The median was found to be an effective operation when the confidence level information is not used.

C. Spectral Width Image-Processing Operation

It has been found that the use of the spectral width confidence level does not improve spectral width image processing. This is because the use of 225-m range gates and periodogram averaging results in very few spurious spectral width estimates at the SNR_w level investigated for this application. Thus, the spectral width image-processing operation F is defined as follows:

$$F(\hat{\sigma}_k) = \text{mean}(\hat{\sigma}_k)$$

The performance of the spectral width image processing is summarized in Fig. 4. The results indicates that the image processing significantly reduces the standard deviation of the spectral width estimate but does not change the underlying mean.

VI. Application of the Processing Algorithms to Real Data: Axial Detection of Wake Vortices with a Ground-Based Lidar

A. Measurement Overview

A Doppler lidar system with a two-dimensional scanner was installed under the flight path into runway 33L at Blagnac Airport, Toulouse, during February and March 2000. The lidar system consists of a 2-μm, coherent pulsed Doppler lidar and a two-dimensional, sinusoidal scanner. The continuously moving scanner allows for only one laser pulse per LOS. The operational parameters of the system are summarized in Table 1.

The lidar system was situated under the glide slope into runway 33L, 530 m from the end of the runway. The instrument landing system guides incoming aircraft to touchdown at a point 300 m along the runway, and so the lidar was 830 m from the average touchdown point. The aircraft landing direction was 330 deg for all of the cases captured by the lidar system. For the cases presented here, the

Table 1 Operational parameters[a] of the lidar system used for ground-based measurement experiments

Lidar system parameters	Value
Laser wavelength	2.02254 μm
Pulse energy	2 mJ
Pulse repetition frequency	500 Hz
Pulse duration ($1/e$ full width)	400 ns
Photodetector sampling frequency	128 Mhz
Horizontal scan range	12 deg
Vertical scan range	3 deg
Number of sinusoidal cycles per image	37
LOS per image	2500

[a]Same parameters were used in all simulation results presented.

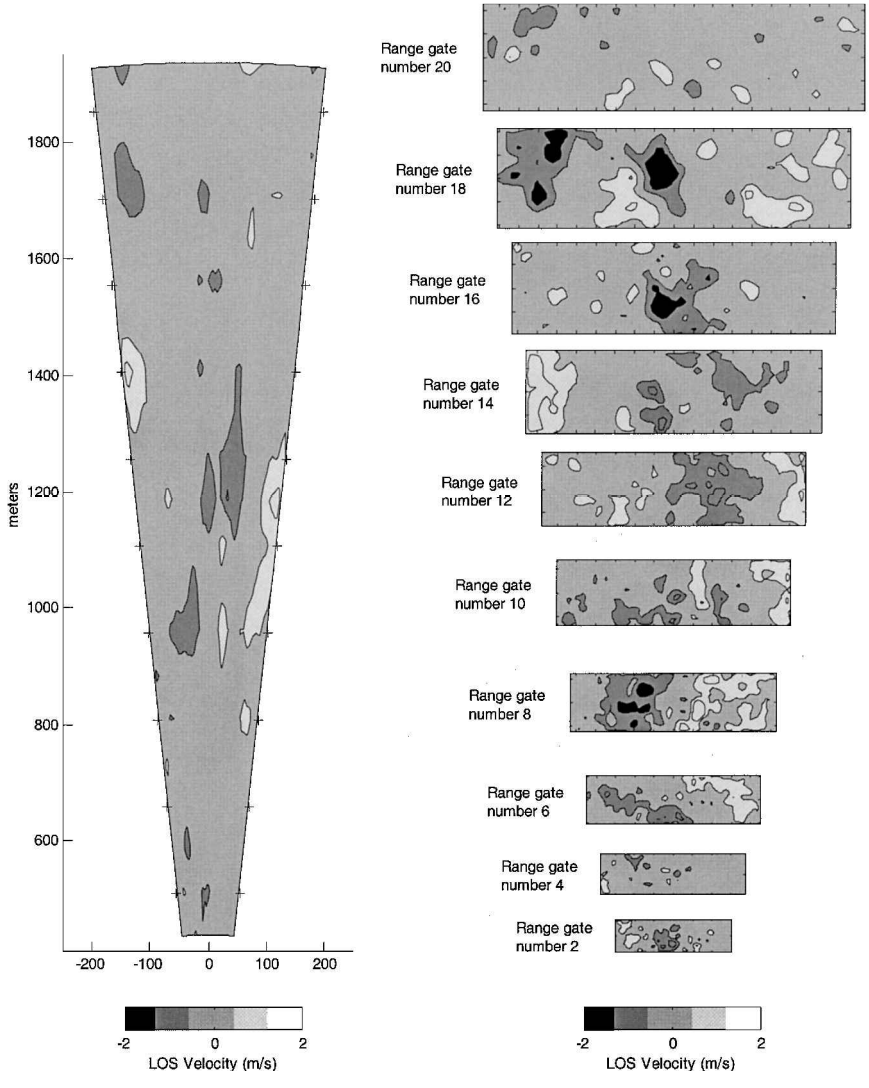

Average top view of the mean radial velocity **Individual range gate images**

Fig. 15 Mean radial velocity images from scan 5 during Airbus 320 landing; + mark centers of range gate images and marks on axes of the range gate images are separated by 20 m.

central axis of the FOV was set to 4 deg from the horizontal. This configuration allows for measurement of the trailing-wake vortices from a close to axial point of view. The measurement geometry is presented in Fig. 7.

B. Data Recording and Processing

For each LOS, the transmitted pulse and return signal are sampled at 128 MHz and stored on a local disc drive. Data storage begins when the landing aircraft is 2–3 km from the Doppler lidar system and continues until 50 s after the aircraft has passed overhead.

The processing algorithms described in this paper have been applied to the data collected during the measurement campaign. Before application of the processing algorithms, the lidar signals were corrected for gain difference caused by the automatic gain control of the system and for frequency shifts caused by jitter in the frequency of the outgoing lidar pulse. Sample results are presented for the following cases: 1) the background wind with no aircraft present, 2) an Airbus A340 approaching to land, and 3) an Airbus A320 approaching to land. All of these cases were measured between 1230 and 1337 hrs on 9 March. The meteorological condition, measured by the local tower at 1220 hrs on that day, was sunny, with a visibility of between 8 and 10 km, and a wind of a less than 3 kn from 330 deg.

The SNR_w performance of the system on the afternoon of 9 March has been estimated from the measured data and is presented in Fig. 8. The estimated performance indicates that the SNR_w is approximately +4 dB at a range of 400 m and that the SNR_w falls off almost linearly to −4 dB at a range of 2000 m.

Reference to Fig. 6 indicates that velocity images contain less than 0.25% spurious estimates after images processing at the lowest end of this SNR_w range and that almost no spurious estimates result at SNR_w greater than −2 dB. Figure 4 indicates that spectral width estimation in the system's SNR_w range accurately reflects the level of turbulence in the range gate. However, Fig. 4 indicates that at the farthest operational range, a decrease in the SNR_w by more than 1 dB, to −5 dB or less, would significantly reduce the spectral width estimation accuracy at that range.

C. Case 1: Background Wind

Figure 9 shows the top view of a complete scan by the system that was carried out at 1230 hrs on 9 March. In addition a number of range gate images are also shown. No aircraft had landed for a number of minutes before this scan was taken. Thus, the scan is of the background wind field only.

The average radial velocity at each range gate has been subtracted from the data before generating these images, to reduce the range of velocity in the image set and, thus, improve contrast in the resulting images. This approach has been found to be beneficial when trying to identify localized axial velocity flows associated with wake vortices. The velocities subtracted are shown in Fig. 10. In general, the average background wind corresponds with the wind speed measured by the Toulouse tower at 1220 hrs of 3 kn (1.5 m/s) from 330 deg.

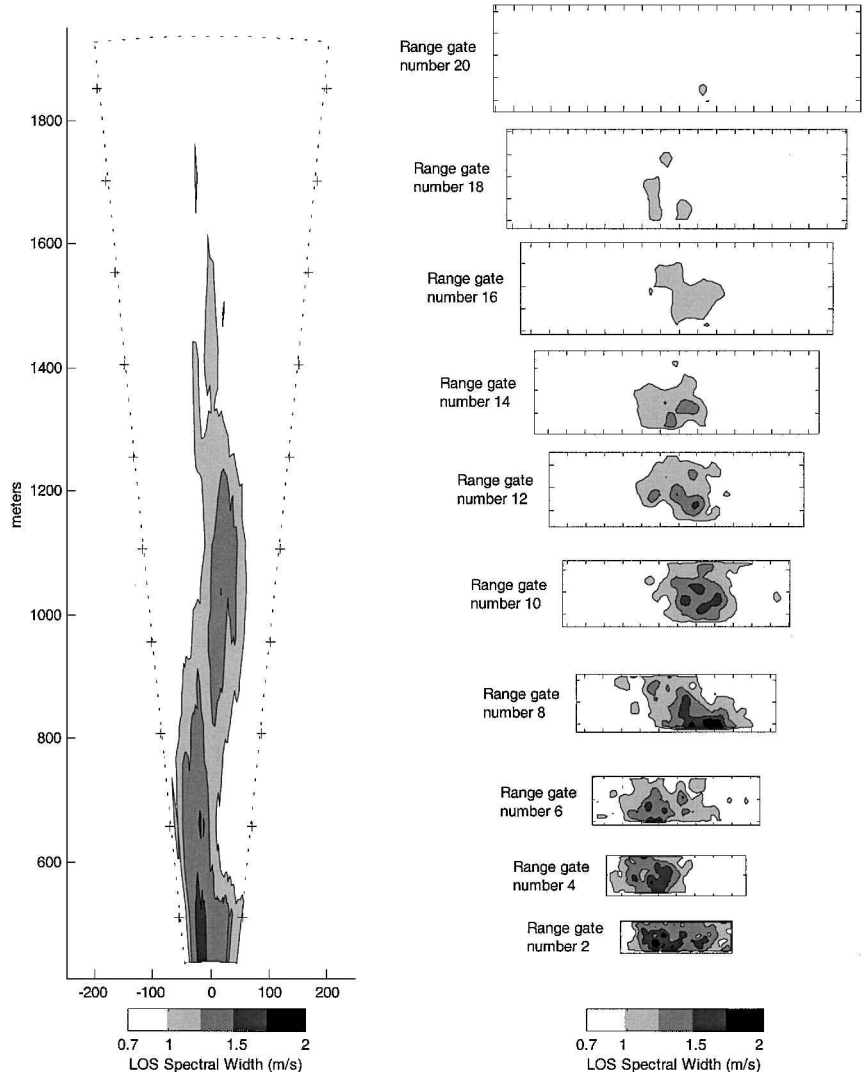

Average top view of the spectral width **Individual range gate images**

Fig. 16 Spectral width images from scan 5 during Airbus 320 landing; + mark centers of range gate images and marks on axes of range gate images are separated by 20 m.

Figure 9 shows some variation in the radial velocity throughout the range gate images, probably due to convective air movement. Figure 11 shows the top view and a number of range gate images of the spectral width results from the same scan. From Fig. 11, it is clear that the spectral width is below 1 m/s in almost all of the FOV for this case.

Figures 9 and 11 are presented as examples of the results achieved when no wake vortices are present in the FOV. Comparison should be made with the results presented in the following sections.

D. Case 2: Airbus A340

Figure 12 shows the average top view of the mean radial velocity and a series of range gate images for the fifth scan of the FOV for this case. As in the preceding case, the average radial velocity of each range gate image has been subtracted to reduce the velocity range in the image set (see Fig. 10).

Figure 13 presents the spectral width results for the same scan in a similar format. A pair of wake vortex induced spectral width signatures are clearly visible, in both the average top view image and in the individual range gate images between 400 and 1400 m. Beyond 1400 m, one of the vortices seems to have dropped out of the FOV, and beyond 1800 m, both vortices seem to have dropped out of the FOV.

By the use of the vortex positions identified in Fig. 13, axial velocities associated with the vortices can be identified in the range gate images of Fig. 12. However, other turbulence structures are present in the radial velocity images, and so axial velocity signatures are not as identifiable as the spectral width signatures.

The aircraft flew over the lidar system approximately 2 s after this scan was completed. When an aircraft speed of 75 m/s is assumed, the vortices age in Figs. 12 and 13 can be calculated to be approximately 4-s old in range gate 1, 5-s old in range gate 2, 6-s in range gate 3, etc., because consecutive range gates are 75 m apart.

The tick marks along the axes of the range gate image, which are separated by 20 m, can be used to estimate the vortex signature separation. Between range gates 4 and 14 the separation of spectral width signatures seems to be stable at approximately 80 m. The approximate vortex ages corresponding to these ranges, can be calculated at 7–15 s. The signature separation is larger than the wing span of an Airbus 340. However, note that the spectral width signatures have not been shown to coincide with the cores of the vortices, and so conclusions about core separation should not be drawn without further investigation.

Figure 14 shows the time evolution of the radial velocity and spectral width range gate images from range gate 6, which is centred at 812 m from the lidar system during the third scan, which begins 12 s after the start of scanning; the vortices are just being formed. At this stage, a small cross section of axial flow toward the lidar is evident. This is probably drag due the aircraft passage. However, as the sequence evolves, weak axial flows in both directions are evident.

The spectral width signatures are clearly evident throughout the sequence. By the fifth scan (scan time of 24 s), when the vortices are approximately 12-s old, the spectral width signatures have separated, to approximately 100 m. This separation is maintained until the vortices are approximately 36-s old. At this stage, the left vortex (on the right from the lidar point of view) has dropped out of the FOV. Thereafter, the right vortex remains in the FOV, and the spectral width signature strengthens until scan 14, at which stage the vortex is 66-s old. By this stage, a strong axial flow is evident in the velocity images. We speculate that the strengthening of the spectral width signature and the inducement of strong axial flows are due to the onset of vortex decay.

E. Case 3: Airbus A320

Figure 15 shows the average top view of the mean radial velocity and a series of range gate images for the fifth scan of the FOV during the landing of an Airbus 320. As in the preceding case, the average radial velocity of each range gate image has been subtracted to reduce the range of velocity in the image set. In this case, the wind velocity has increased to 7 kn or 3.5 m/s (Fig. 9). This is a significant increase from the tower measurement of 3 kn taken 40 min earlier.

Figure 16 presents the spectral width results for the same scan in a similar format. Spectral width signatures are clearly visible in both the average top view image and the range gate images, although, unlike the A340 case, separate spectral width signatures are not visible for two vortices.

As in the preceding case, the vortex positions can be identified via the spectral width images, and then axial velocities associated with the vortices can be identified in some of the range gate images of Fig. 15. However, other turbulence structures are again present in the radial velocity images. The spectral width signatures are clearly more useful for detecting wake vortices.

The aircraft flew over the lidar system shelter approximately 9 s before this scan began. Assuming an aircraft speed of 75 m/s, the vortices' age in Figs. 15 and 16 can be calculated to be approximately 16-s old in range gate 2, 18-s old in range gate 4, etc.

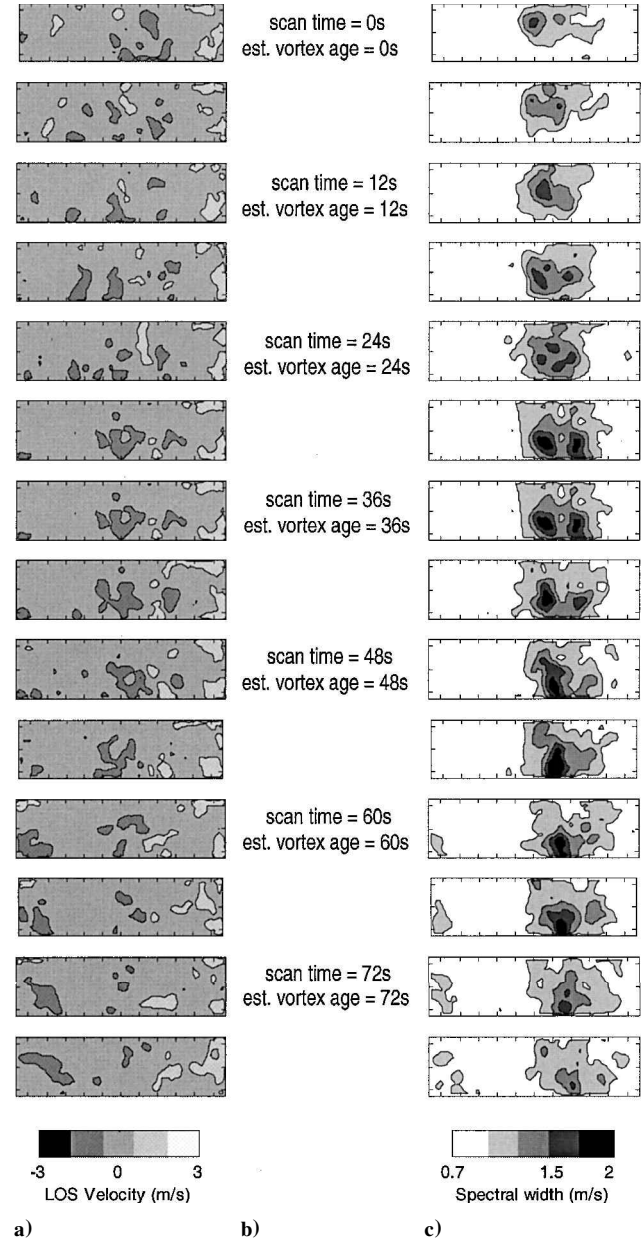

Fig. 17 Time evolution of images from range gate 10, centered 1112 m from lidar system, during Airbus 320 landing; marks are 20 m apart on both axes: a) mean radial velocity variation from the average range gate velocity, b) approximate start time of each scan and the estimated vortex age (estimate from the flyby time) and c) spectral width.

Figure 17 shows the time evolution of the radial velocities and spectral width range gate images from range gate 10, which centered at 1112 m from the lidar system. The mean velocity image sequence does not show any clear conclusive vortex signatures. However, the spectral width signatures are clearly evident throughout the sequence. At a scan time of 30 s, by which time the vortices are also approximately 30-s old, a pair of the spectral width signatures becomes evident. Two separate signatures remain evident for a further 12 s, and thereafter the left vortex (right-hand vortex from the lidar point of view) seems to either decay or suddenly sink out of the FOV. The other vortex remains in the FOV, and the spectral width signature begin to weaken from ages 60 s.

VII. Conclusions

The processing approach, which was developed using simulation techniques, performed well when applied to data from ground-based measurements. Sample results presented demonstrate that robust detection of trailing wake vortices from an axial point of view has been achieved for A320 and A340 aircraft. In particular, the spectral width signatures seem to be a robust axial indicator of wake vortex presence. Cases involving other types of aircraft landing at Toulouse airport have also been processed. Similar detection results have been achieved for a Boeing 737, an MD-80, an Airbus A300-600 Super Transporter, and a Fokker 100 aircraft.

These results should be interesting to any researchers who are involved in the development of ground-based wake vortex tracking systems. In particular, these results indicate that a single axially oriented ground-based Doppler lidar system, using the processing approach described here, could be used to monitor the critical region of an aircraft's approach, which extends from near the aircraft touchdown zone to a distance of approximately 2 miles from the runway.

If a lidar system with similar performance to that outlined in Table 1 could be mounted in a commercial aircraft, the results presented here indicate that robust wake vortex detection with an airborne system is feasible. This approach, which was proposed in the Multifunction Future Laser Atmospheric Measuring Equipment project, would enable pilots with an autonomous wake vortex detection and avoidance capability. Such a system could be an important component in a framework that would allow for a reduction in aircraft separation under appropriate conditions without compromising safety levels.

Acknowledgments

The work presented here was performed in the Multifunction Future Laser Atmospheric Measuring Equipment (MFLAME) project under Brite Euram Contract BRPR96-182, which was supported by the European Communities Fourth Framework Research Programme. The authors acknowledge the contributions of the other partners in the MFLAME consortium. In particular we acknowledged the contribution of Hubert Combe of SEXTANT, who coordinated the MFLAME program and Alex Corjon and Denis Darracq of Centre Europeen de Recherche et de Formation Avancée en Calcul Scientifique, who carried out the LES simulations.

References

[1]Hallock, J. N., "Aircraft Wake Vortices: An Assessment of the Current Situation," Volpe National Transportation Systems Centre, Rept. DOT-TSC-FAA-90-6, Cambridge, MA, Jan. 1991.

[2]Vicroy, D., Brandon, J., Greene, G., Rivers, R., Shah, G., Stewart, E., and Stuever, R., "Characterizing the Hazard of a Wake Vortex Encounter," AIAA Paper 97-0055, Jan. 1997.

[3]Rossow, R. V., and Tinling, B. E., "Research on Aircraft/Vortex-Wake Interactions to Determine Acceptable Level of Wake Intensity," *Journal of Aircraft*, Vol. 25, No. 6, 1988, pp. 481–492.

[4]Tatnall, C., "Investigation of Candidate Sensor-Observable Wake Vortex Strength Parameters for the NASA Aircraft Vortex Spacing System (AVOSS)," NASA CR-1998-206933, March 1998.

[5]Brockman, P., Barker, B., Koch, G., Dung, P., Britt, C., and Petros, M., "Coherent Pulse Lidar Sensing of Wake Vortex Position and Strength, Winds and Turbulence in the Terminal Area," Tenth Biennial Coherent Laser Radar Technology and Applications Conf., Mt. Hood, OR, Optical Society of America, June 1999, pp. 12–25.

[6]Hannon, S. M., and Thompson, A. J., "Aircraft Wake Vortex Detection and Measurement with Pulsed Solid-State Coherent Laser Radar," *Journal of Modern Optics*, Vol. 41, No. 11, 1994, pp. 2175–2196.

[7]Koepp, F., "Doppler Lidar Investigation of Wake Vortex Transport Between Closely Spaced Runways," *AIAA Journal*, Vol. 32, No. 4, 1994, pp. 805–810.

[8]Darracq, D., Corjon, A., Ducros, F., Keane, M., Buckton, D., and Redfern, M., "Simulation of Wake Vortex Detection with Airborne Doppler Lidar," *Journal of Aircraft*, Vol. 37, No. 6, 2000, pp. 984–993.

[9]"*Aeronautic Related Research: Synopsis of Current Projects Selected Under the 1995 Call for Proposals*," Official Publ. of the European Communities, Luxembourg, 1996, p. 226.

[10]Huffaker, R. M., and Hardesty, R. M., "Remote Sensing of Atmospheric Wind Velocities Using Solid-State and CO2 Coherent Laser Systems," *Proceedings of the IEEE*, Vol. 84, No. 2, 1996, pp. 181–204.

[11]Brown, C. E., "Aerodynamics of Wake Vortices," *AIAA Journal*, Vol. 11, No. 4, 1973, pp. 531–536.

[12]Batchelor, G., "Axial Flow in Trailing Line Vortices," *Journal of Fluid Mechanics*, Vol. 20, No. 4, 1964, pp. 645–658.

[13]Zrnic, D. S., "Estimation of Spectral Moments for Weather Echoes," *IEEE Transactions on Geoscience Electronics*, Vol. GE-17, No. 4, 1979, pp. 113–128.

[14]Proakis, J. G., and Manolakis, D. G., *Digital Signal Processing, Principles, Algorithms and Applications*, 3rd ed., Prentice–Hall, Upper Saddle River, NJ, 1996, p. 106.

[15]Frehlich, R., "Effects of Wind Turbulence on Coherent Doppler Lidar Performance," *Journal of Atmospheric Science and Oceanic Technology*, Vol. 14, No. 1, 1997, pp. 54–75.

[16]Salamitou, P., Dabas, A., and Flamant, P. H., "Simulation in the Time Domain for Heterodyne Coherent Laser Radar," *Applied Optics*, Vol. 34, No. 3, 1995, pp. 449–506.

[17]Doviak, R., and Zrnic, D., *Doppler Radar and Weather Observations*, 2nd ed., Academic Press, London, 1993, p. 400.